Ocean Engineering 172 (2019) 562–574

Contents lists available at ScienceDirect

Ocean Engineering

journal homepage: www.elsevier.com/locate/oceaneng

Computational and experimental modelling study of the unsteady airflow over the aircraft carrier HMS Queen Elizabeth

N.A. Watson[a], M.F. Kelly[a], I. Owen[a,*], S.J. Hodge[b], M.D. White[a]

[a] School of Engineering, University of Liverpool, UK
[b] Flight Simulation, BAE Systems, Warton Aerodrome, UK

ARTICLE INFO

Keywords:
Aircraft Carrier
Airwake
Ship aerodynamics
Delayed detached eddy simulation
CFD validation
Acoustic Doppler velocimetry

ABSTRACT

This paper describes a comprehensive experimental and computational modelling study of the aerodynamic environment around the UK's new Queen Elizabeth Class (QEC) aircraft carriers. The study has been performed to support the integration of the F-35B Lightning II multi-role fighter with the UK Royal Navy's flagship, HMS Queen Elizabeth. Unsteady airwakes have been generated using Computational Fluid Dynamics (CFD) and have been incorporated into the F-35/QEC Integration Flight Simulator at BAE Systems Warton and into the HELI-FLIGHT-R research simulator at the University of Liverpool.

A small-scale experiment has also been conducted in which a 1.4 m long (1:200) scale model of the QEC was submerged in a water channel and Acoustic Doppler Velocimetry was used to measure the unsteady flow around the ship. Delayed Detached Eddy Simulation CFD was used to model the flow in the water channel and the computed unsteady flow field has been compared with the experimental measurements. The results show generally excellent agreement between the model-scale experiment and CFD. Building on this, full-scale 30-s CFD airwakes have been generated for the nearfield area surrounding the QEC, and for about 400 m astern of the ship to capture the disturbed air flow along the fixed-wing approach glideslope.

1. Introduction

The first of the United Kingdom's two new aircraft carriers, HMS Queen Elizabeth, shown in Fig. 1, was commissioned at the end of 2017, and at the time of writing has already successfully conducted sea-trials and rotary-wing flight testing; the second carrier of its class, HMS Prince of Wales, is at an advanced stage of construction. At 65,000 tonnes each, with a length of 280 m and a beam of 73 m, they are the largest and most capable warships ever built for the Royal Navy.

The Queen Elizabeth Class (QEC) carriers have been primarily designed to operate the Lockheed Martin F-35B Lightning II which is the world's first supersonic stealth Short Take-Off and Vertical Landing (STOVL) fighter aircraft (Bevilaqua, 2009). Characteristic features of the QEC, as can be seen in Fig. 1, include the twin island superstructure, and the ramp, or “ski-jump”, at the bow to facilitate short take-off. The forward island is primarily for ship control and navigation and the aft island houses the Flying Control, or FLYCO, area which is primarily for directing flight operations. The concurrent development of the QEC and F-35B has presented a unique opportunity to deploy modelling and simulation to optimise the aircraft-ship interface and to maximise the combined capabilities of these two assets (Lison, 2009). As well as the fixed-wing F-35B, it is expected that the QEC carriers will also operate rotary-wing assets such as Merlin, Wildcat, Chinook and Apache helicopters.

The University of Liverpool (UoL) has been at the forefront of modelling and simulation research to provide a better understanding of the air flow environment around ships and how it affects the flying qualities of the ship's aircraft and pilot workload (Owen et al., 2017). The disturbed air flow in the lee of a ship's superstructure is created by a combination of the ship's forward speed and the prevailing wind, and is known as the ‘airwake’. To enable the airwake to be included in the simulation environment, it is modelled using Computational Fluid Dynamics (CFD). The majority of the research conducted by the UoL in this area has been for single-spot frigates and destroyers, and the two principal aims of this ongoing work are to (i) create a flight simulation environment for realistic helicopter launch and recovery operations (Hodge et al., 2012), and (ii) develop guidance for ship designers to minimise the effect of ship superstructure aerodynamics on helicopter operations (Forrest et al., 2016); both aims being directed towards maximising operational capability and reducing pilot workload during helicopter launch and recovery.

Currently, the UoL is working with BAE Systems to develop a

* Corresponding author.
E-mail address: i.owen@liv.ac.uk (I. Owen).

https://doi.org/10.1016/j.oceaneng.2018.12.024
Received 18 September 2018; Received in revised form 20 November 2018; Accepted 5 December 2018
0029-8018/ © 2018 The Authors. Published by Elsevier Ltd. This is an open access article under the CC BY license (http://creativecommons.org/licenses/BY/4.0/).

Fig. 1. HMS Queen Elizabeth aircraft carrier during sea trials (Royal Navy Imagery Database, 2018).

simulation of the aerodynamic environment around the QEC for the fixed-wing F-35B/QEC Integration Simulator operated by BAE Systems (Hodge and Wilson, 2008). Also, with joint funding from the UK's Engineering and Physical Sciences Research Council and BAE Systems, UoL is creating a simulation of the QEC to be implemented into its generic research simulator the HELIFLIGHT-R (White et al., 2013).

This paper describes the results of a comprehensive study into the air flow over and around the QEC. A small-scale experiment has been carried out in which a 1.4 m long (1:200) scale model of the QEC was submerged in a water channel and Acoustic Doppler Velocimetry (ADV) was used to measure the three components of velocity in the flow around the ship; the inlet flow in the water channel had a uniform velocity profile. A selection of results are reported with the model ship aligned with the flow, so that it was equivalent to a headwind, and with the ship model aligned so the oncoming flow direction was 10° from starboard. CFD was used to model the flow in the water channel and the computed flow field has been compared with the experimental measurements. The results presented in this paper show generally excellent agreement between the model-scale experiment and model-scale CFD; the average difference between the measured and computed velocities was less than 5%. Building on this, CFD airwakes have also been computed for the air flow around the full-scale QEC, and for 400 m astern of the ship to capture the disturbed air flow along the fixed-wing aircraft approach path. The full-scale CFD flow field has been computed with an inlet velocity profile that is representative of an oceanic atmospheric boundary layer. Despite the larger CFD model having different inlet conditions and a higher Reynolds number, the results show that there is still reasonable agreement between the full- and model-scale velocity flow fields, with observed differences being, on average, about 6%. Finally, the full-scale CFD has been used to compute the airflow over the ship in oblique and beam winds where the twin island configuration leads to a more complex flow environment over the ship's flight deck.

2. The ship airwake

Extensive research has previously been carried out at UoL (Owen et al., 2017), largely focussed on airwake modelling for “single-spot” ships (i.e. frigate-sized vessels). The QEC aircraft carriers are significantly larger multi-spot platforms, each possessing an approximately four-acre flight deck, and with a requirement to operate both fixed- and rotary-wing aircraft. The generation of time-accurate CFD airwakes for a multiple-spot aircraft carrier requires a significant increase in computational power when compared with the CFD solution for a single-spot frigate. To adequately resolve the turbulent length scales passing over a ship's flight deck, it is necessary for the mesh size

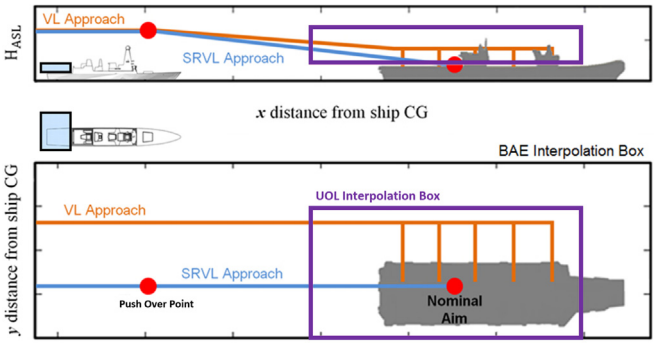

Fig. 2. CFD focus region and export domains for UoL and BAE Systems flight simulators.

in the region of interest to be sufficiently refined. It is therefore necessary for the grid density to be carefully controlled in the CFD region of interest, or “focus region”.

In the case of CFD for aircraft operations to/from the QEC, the focus region is the area through which aircraft will pass on approach to the ship during the Vertical Landing (VL), which is the primary means of recovery, the Shipborne Rolling Vertical Landing (SRVL) and the Ski-jump Take-Off (STO). SRVL is a new recovery method unique to the UK F-35B/QEC combination and involves the aircraft recovering along a 7° glideslope over the stern of the ship, at a low forward speed, and stopping on deck using the wheel-brakes (Cook et al., 2010; Atkinson et al., 2013). The advantage of SRVL over the traditional ‘hover-translate-land’ technique is an additional capacity to recover to the ship at higher gross weights (e.g. with more fuel and/or stores), by using wing-lift to augment the lift available from the propulsion system. Fig. 2 shows the CFD focus region which extends approximately 1.5 ship lengths aft of the ship. Also shown in Fig. 2 are the interpolation boxes, or export domains, used in the BAE Systems (black box) and UoL (purple box) flight simulators, compared with that used in previous experiments at UoL focussed on single-spot frigates (light blue filled box). The unsteady velocity components generated by the CFD models, within these interpolation boxes, are interpolated onto a uniform grid and exported to the flight simulator host software as look-up tables. Compared with the previous studies, focussed on single-spot frigates, the difference in the export volumes graphically illustrates the size of the challenge faced during implementation of the aircraft carrier airwakes, in terms of computational resources and real-time data storage and manipulation.

The volume of flow that has been investigated, both experimentally and computationally, corresponds to the focus region shown in Fig. 2. The Reynolds number of the experimental flow, based on the length of the carrier model was approximately 1.4×10^6, compared with approximately 2×10^8 for the full-scale ship with a wind speed of 10 m/s (~20 knots). In experimental bluff body aerodynamics, especially where the body has sharp edges, it is common practice to assume that the flow characteristics are independent of Reynolds number; this is because the flow separates cleanly from sharp edges, unlike, for example, the separation from the curved surface of an aerofoil. For the flow around rectangular blocks, ESDU (Engineering Sciences Data Unit, 1978) notes that the force coefficients do not change over the Reynolds number range of 10^4 to 10^6; however, if the blocks are long in the direction of the flow then there will be a reattachment that is seen to be Reynolds number dependent. As shown in Fig. 1, the leading edges of the QEC flight deck and the ski-jump both have a radius, a precaution to prevent flow separation; it can also be seen from Fig. 1 that the front of the ship is rather blunt. Drawing upon studies into the aerodynamics of large road vehicles (Cooper, 1985; Hucho et al., 1976), the rounded leading edge of the small-scale model of the QEC can be expected to have flow separation, while the full-scale ship will not; this was one reason why the CFD methodology was applied to both the experimental

and full-scale situations, the other being that the experimental inlet flow had a uniform velocity profile, whilst at full-scale a profile approximating the atmospheric boundary layer over the open ocean was applied at the inlet.

Research into ship airwakes and their integration with piloted flight simulation over the past decade or more has shown that it is essential to create the airwakes using time-accurate CFD, so that the irregular time-varying velocity components can be captured and applied to the aircraft flight dynamics model to provide a realistic experience for the pilot, in terms of handling qualities and pilot workload (Roper et al., 2006; Hodge et al., 2012). The application of the CFD in the flight simulator normally employs around 30 s of unsteady three-dimensional velocity components, extracted from within a specified domain over and around the ship; the 30 s airwake time histories are then looped in the simulation to create a continuously unsteady flow field (Hodge et al., 2012). A time-accurate CFD technique is therefore required and Detached-Eddy Simulation (DES) lends itself very well to modelling unsteady flows, such as those associated with bluff bodies, which are dominated by both quasi-periodic large-scale structures and chaotic small-scale turbulent features.

DES utilises the eddy-resolving power of Large-Eddy Simulation (LES) in areas of large separation, and a Reynolds Averaged Navier-Stokes (RANS) approach in the boundary layer (Spalart, 1997); this is achieved through the replacement of the distance to the wall term, d, in the underlying Spalart-Allmaras (S-A) turbulence model by:

$$\tilde{d} = \min(d, C_{DES}\Delta) \quad (1)$$

The modified turbulent length scale, $\tilde{d}$, which drives the production of eddy-viscosity is then linked to the local grid spacing, Δ. In regions where the grid is fine enough, eddy-viscosity production is limited, allowing medium to large scale turbulent structures to be explicitly resolved using LES. This reduction in eddy-viscosity prevents artificial dampening of the flow field perturbations by the turbulence model and allows turbulent structures to propagate.

In a typical DES simulation a RANS sub-grid scale model with a low-Reynolds number correction is utilised throughout the boundary layer; however as the turbulent length scale is linked to the local grid spacing care must be taken so that the streamwise grid spacing is longer than the boundary layer height to ensure LES is not resolving the flow. Therefore, in areas of an ambiguous grid definition, or a large boundary, LES may be activated prematurely inside the boundary layer, where the grid is not fine enough for LES to resolve the velocity fluctuations. This reduction in eddy-viscosity and modelled Reynolds stresses due to the grid spacing is known as Modelled Stress Depletion and it can also result in Grid Induced Separation in areas where the unresolved Reynolds stresses lead to an artificially reduced skin friction coefficient (Menter et al., 2004).

Retaining an unambiguous grid near the wall is a challenge for the complex geometry of the ship and the full range of wind azimuths. Therefore, Delayed Detached-Eddy Simulation (DDES), which is a modified version of DES, was used in the present study. DDES defines a more general form of the local grid spacing by combining local grid scales and the wall distance (Spalart et al., 2006).

One concern with the application of CFD to ship airwake modelling is the potential for artificial dissipation of turbulent energy, especially in the region downstream of the ship; this may be attributed in part to the overly dissipative sub-grid scale model applied when the turbulent length scale is less than the grid spacing in LES mode (Spalart, 2001). A sufficiently fine grid is therefore required in the wake region of the ship to minimise this unphysical dissipation, and this was achieved by constraining the grid elements to a maximum size when producing the computational mesh in the focus region. Further dissipation in the form of numerical diffusion, a common issue with unstructured grids, was reduced through the application of a third-order Monotone Upstream-Centred Schemes for Conservation Laws (MUSCL) numerical discretisation scheme; this scheme is a blend of a central differencing scheme and second-order upwind scheme (ANSYS and Inc, 2016).

DDES is therefore particularly well suited to ship airwake modelling because in regions of interest, where the accurate capture of turbulent features is important, turbulence is explicitly resolved by the grid, whereas in regions of irrotational flow, close to walls, the standard SST k-ω RANS model is used. DDES has relatively modest computational requirements compared with LES as it relaxes near-wall mesh requirements. The ANSYS Fluent finite-volume unstructured solver was used to perform the numerical simulations.

3. Experimental study

Detailed digital drawings of the QEC were used to create both the physical small-scale model and the geometry for the CFD computations. The 1.4 m long experimental model was manufactured using 3-D printing techniques. The hull was manufactured from ABS (Acrylonitrile Butadiene Styrene) in three interlocking sections using Fused Deposition Modelling, as were the ski-jump and islands; the main mast located on the aft island was manufactured from cobalt chrome using Direct Metal Laser Sintering, due to the higher stiffness required for this slender component. All the manufacturing was carried out at BAE Systems' Additive Layer Manufacturing Centre. The ABS components, particularly the sloping ski-jump, required some additional finishing to obtain a smooth surface due to the effect of rasterization which is inherent to the additive layering process. The assembled ship model is shown in the upper part of Fig. 3. The hull was designed to be hollow to reduce manufacturing time and cost, as well as the overall weight. Five suction cups were attached to the underside of the hull sections to secure the model to the smooth floor of the water channel using a vacuum pump; a CAD model showing the suction cups (in blue) attached to the underside of the QEC model can be seen in the lower part of Fig. 3.

The experiments were carried out in a recirculating water channel, shown schematically in Fig. 4. The working section is 3.7 m long, 1.4 m wide, and has an adjustable floor to give water depths between 0.15 and 0.85 m; for this study the water depth was 0.8 m. While water speeds can be carefully controlled up to a maximum speed of 6 m/s, for the current experiments an inlet velocity of 1 m/s was adopted to minimise disturbance at the generally smooth water surface in the open channel. A brass honeycomb flow-straightener in combination with a contraction upstream of the open channel working section ensures a uniform velocity profile at the section entry, while a water jet injection at the start of the working section adds flow to the free surface to

Fig. 3. Assembled 1:200 scale model of HMS Queen Elizabeth.

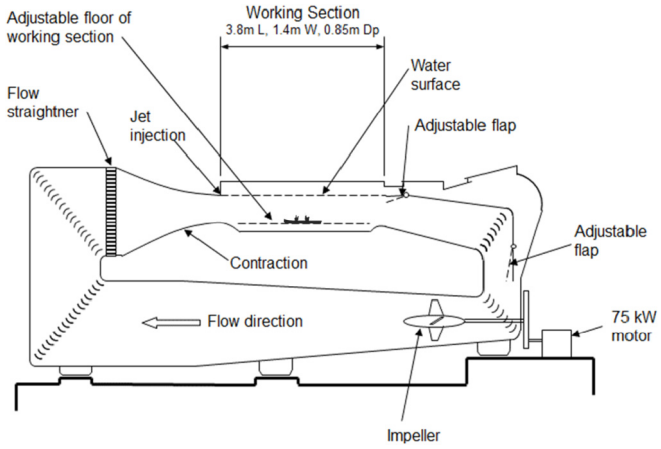

Fig. 4. University of Liverpool recirculating water channel.

maintain the uniform velocity profile at the surface (Millward et al., 1980). For the small-scale CFD the ship airwake was therefore computed with a uniform inlet velocity profile. With the QEC model aligned in the flow direction, the working section blockage was approximately 3.2%.

Velocity measurements in the water channel were made using a Nortek Vectrino + ADV. Three-dimensional laser Doppler anemometry was considered, as was particle imaging velocimetry, but optical access to the flow within the water channel proved to be problematic. An ADV is an acoustic velocity sensor, able to measure three-dimensional velocity in a flow based upon small variations in acoustic signal frequency arising from the Doppler effect (Kraus et al., 1994). The two Nortek Vectrino + ADV probes used in this study (Fig. 5) each consist of an acoustic signal transmitter and four receivers, which are orientated to measure the velocity of particles suspended in the fluid at a distance of 50 mm from the transmitter, thereby minimising any interference with the flow. Velocities are measured across a small cylindrical sampling volume, the size of which can be adjusted according to experimental conditions (Lohrmann et al., 1994). During this study, the cylindrical sampling volume for each probe was set at a diameter of 6 mm and a length of 7 mm, with the mid-point located 50 mm from the acoustic transmitter, as shown in Fig. 5.

ADVs have been shown to provide mean three-component velocities to within 1% of validation data in a range of laboratory and field conditions (Lohrmann et al., 1994; Lane et al., 1998; Lopez and Garcia, 2001), however the presence of signal noise can impair the ability of the ADV to report accurate turbulent statistics. The noise present in ADV velocity signals results from a combination of Doppler noise, signal aliasing, and velocity shear across the sampling volume (Voulgaris and Trowbridge, 1998), with Doppler noise having the largest impact upon measured data in the two velocity components normal

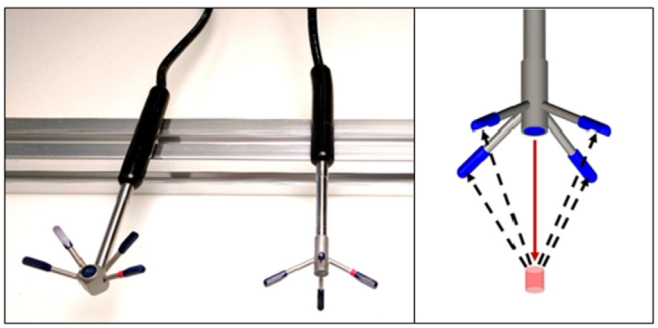

Fig. 5. Nortek Vectrino + ADV sideways- and downwards-looking probes and schematic showing measurement volume relative to the probe transmitter and receivers.

to the acoustic transmitter (Chanson et al., 2007). As Doppler noise is characterised as unbiased white noise, mean three-component velocities are left unaffected. However, accurate turbulent statistics cannot be recovered from the signals of the two velocity components normal to the probe's transmitter due to increased levels of Doppler noise. As a result, only the three-component mean velocities and turbulent statistics in the flow component aligned with the transmitter can be reliably obtained for one probe alignment; for this reason, the current study used the two differently oriented probes shown in Fig. 5 to obtain turbulence statistics in two components.

The two probes were first used in an open channel to compare their readings. Mean velocities were found to agree within 1%, consistent with the manufacturer's specification. The sideways-looking probe was in error when faced into the flow, due to the probe interfering with the flow, and therefore it was not used in this orientation. As unsteady turbulence measurements are only reliable in the direction of the acoustic transmitter, this means that, whilst three mean velocity components could be measured, reliable turbulence measurements could only be obtained in the lateral and vertical components of flow. Measurements of inlet turbulence by the two probes showed a turbulence intensity of 1% in the lateral and vertical components, indicating that the incoming flow had isotropic turbulence, as expected.

To facilitate the large number of ADV point measurements that were required, and to ensure positional accuracy and repeatability, a specially designed three-dimensional electronic programmable traverse system was manufactured and assembled above the water channel. In total, approximately 1500 measurements were made for each ship orientation, and each measurement was sampled at 200 Hz for a period of 60 s, thus recording 12,000 individual samples per velocity time-history. This sampling record size is significantly larger than the 5000 samples required to yield minimum errors on first and second-order statistical moments (i.e. mean and standard deviations) of the velocity components (Chanson et al., 2007). The positional accuracy of the traverse was 0.1 mm and the datum of the probe measurement volume was located to an accuracy of 1 mm in the x, y and z direction by using the in-built ability of the probe to quantify the distance of the sampling volume from a solid surface, e.g. the ship model. The positional accuracy of the probe within the flow was therefore assumed to be approximately 1.1 mm, and this was regularly checked when the probe came close to the ship surface.

4. Small-scale CFD study

For the small-scale CFD study the computational domain was given the same height and width as the water channel, and the length of the domain was made larger by 2.5 m to minimise any spurious effects from the inlet and outlet boundary conditions.

The detailed ship geometry was simplified so that at full-scale all features less than 0.5 m were removed. The ship surface was specified as a no-slip boundary, as were the side walls and floor of the water channel; the free surface of the water channel was set as a slip surface, i.e. frictionless with no velocity gradient normal to the surface. The flow velocity at the inlet of the domain was set as a uniform 1.0 m/s, to replicate the experimental conditions, and the outlet plane was set as an outflow boundary condition. From previous experience (Forrest and Owen, 2010), the surface cell size normally applied to a full-scale ship is approximately 0.3 m; for the small-scale model this proportion was retained and so was set at 1.485 mm.

Twelve prism layers were applied on the non-slip surfaces. Using a non-dimensionalised first layer height ($Y+$) of 30 and a growth ratio of 1.2, the height of the next layer was calculated using the exponential prism growth law. A mesh density box was created to represent the focus region (shown earlier in Fig. 2) within which the elements were restricted to a maximum size of 5 mm (equivalent to 1 m at full-scale), allowing the flow to be resolved with a higher fidelity in the region of interest over the deck and astern of the ship. For the headwind case the

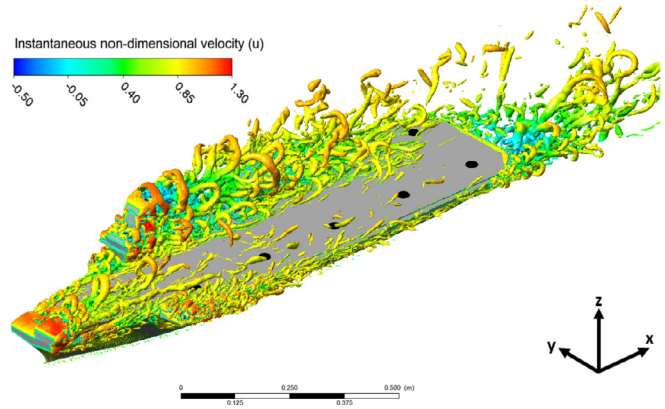

Fig. 6. Headwind flow over QEC model presented as instantaneous isosurfaces of Q-criterion coloured by *u*-velocity.

focus region was aligned with the axis of the water channel, while to create the equivalent of a wind coming 10 degrees off the starboard side the rectangular box was positioned mid-channel and rotated anticlockwise through 10°. These configurations each had a total mesh size of approximately 90 million cells.

The flow solution was initiated as steady state with 3000 iterations, the unsteady solution was then run with a time step of 0.001 s (equivalent to approximately 100 Hz at full-scale). The CFD solution requires a period of time to settle to a repeatable unsteady solution; this period was typically 10 s, allowing a water particle to pass through the working section at least 2.5 times, and thereby allowing periodic flow features to fully develop. For the small-scale solution the unsteady flow field was solved for 3 s, which in total required around 30 days computing time running on 128 processors of a High Performance Computing (HPC) cluster.

4.1. Headwind

Fig. 6 shows the instantaneous flow over the ship where the turbulent vortical structures are presented as Q-criterion isosurfaces. The Q-criterion is defined as the second invariant of the velocity gradient tensor ∇u and is used as a vortex identification method; a positive value of Q is a region within the flow where the vorticity magnitude is larger than the strain-rate magnitude and is denoted as a vortex (Hunt et al., 1988).

The results presented in Fig. 6 were also used to inform the experiments. From an operational perspective the areas of interest are the landing spots, which are along the flight deck and are indicated as black dots in Fig. 6. Spot 1 is the most forward, followed by spots 2 to 5; spot 6 is alongside spot 5 and situated behind the aft island. In a headwind, there is little disturbance in the flow over the landing spots; the exception being spot 6 which is in the turbulent wake in the lee of the islands. In contrast, from the perspective of comparing experimental data with the CFD solution, the areas around the bow of the ship, the islands and astern of the ship are of greater interest; experimental velocity measurements were therefore concentrated in these key areas. Also shown in Fig. 6 are the *x*, *y*, *z* axes relative to the ship. The longitudinal axis, or *x*-axis, is parallel to the ship's centreline (positive towards the stern); *y* is athwartships (positive starboard); and *z* is in the vertical direction (positive upwards). The corresponding velocities in these axes are *u*, *v* and *w*, respectively.

Fig. 7 shows the unsteady airwake at an instant in time as contours of the streamwise *u*-velocity component. The vertical plane is parallel to the ship's longitudinal axis and passes through the centre of the islands and, therefore, is offset to the starboard side of the ski-jump.

Fig. 8 shows a comparison between the measured and computed values of the mean streamwise velocities along vertical lines at various

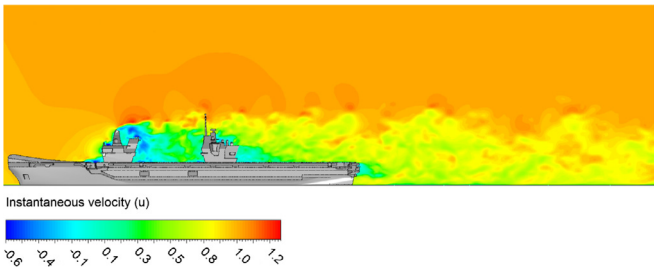

Fig. 7. Contours of instantaneous *u*-velocity components (m/s) in a vertical plane through the centre of the islands.

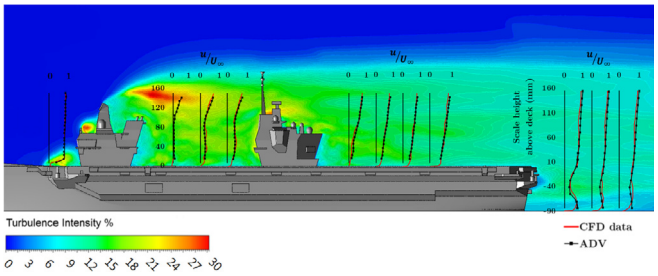

Fig. 8. Comparison of experimental and CFD *u*-velocity components in a plane through the centre of the islands.

positions over and astern of the ship, again in a plane through the centre of the islands. In this case the airwake is illustrated by contours of turbulence intensity which, throughout this study, is defined as the Root Mean Square (RMS) of the turbulent velocity fluctuations divided by the freestream flow velocity, i.e. not the local velocity. For example, the turbulence intensity presented as contours in Fig. 8 is calculated by Eqn. (1), where u', v', w' are the fluctuations in the three velocity components *u*, *v*, *w*.

$$Ti = \frac{\sqrt{\frac{1}{3}(u'^2 + v'^2 + w'^2)}}{U_\infty} \tag{2}$$

It can be seen in Fig. 8 that ahead of the forward island the *u*-velocity profile above the deck is largely undisturbed, whereas in the lee of each of the islands and at the stern of the ship there is a significant velocity deficit compared with the freestream. Also, referring to the contours of turbulence intensity, the turbulence between the islands is of the order of 20%. As can be seen in Fig. 8 the agreement between the CFD (red line) and the experiment (black line) is mostly very good.

Fig. 9 compares the experimental and CFD values of the lateral, *v*, and vertical, *w*, mean velocity components and turbulence intensities at various positions behind the islands. In this case the turbulence intensity is the fluctuating velocity component divided by the mean freestream, e.g. w'/U_∞, consistent with Eqn. (2). There is a greater proportional difference between the CFD and the experiment than in Fig. 8, however, it should be noted that the mean velocities in these directions are very small, mostly less than 0.1 m/s.

Fig. 10 shows a comparison of the mean *u*-velocity component at three positions astern of the ship on the ship centreline (i.e. $y = 0$) and, therefore, in a different plane to Figs. 8 and 9; contours of turbulence intensity are also shown. There is again good agreement between the CFD and the experiment, and the reverse flow region in this plane can be clearly seen. The higher levels of turbulence indicate the existence of a shear layer between the main flow and the recirculation zone.

Fig. 11 shows the lateral and vertical velocity components along the vertical line in Fig. 10 which is closest to the ship. The negative vertical velocity component, *w*, can be clearly seen. Because the line is at the centreline of the ship, the lateral velocity component, *v*, might be expected to be close to zero; however, the ship is not symmetrical and so neither is the airwake astern of the ship. The comparison between the

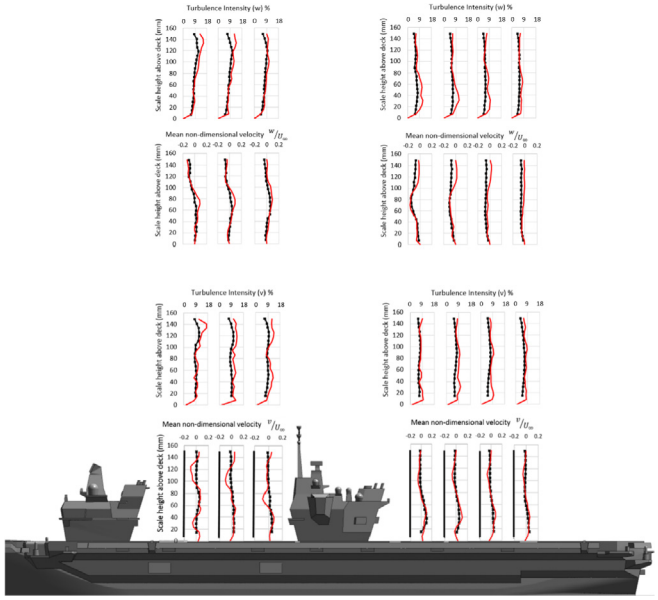

Fig. 9. Comparison of experimental and CFD mean *v*- and *w*-velocity and RMS velocity components in the lee of the islands.

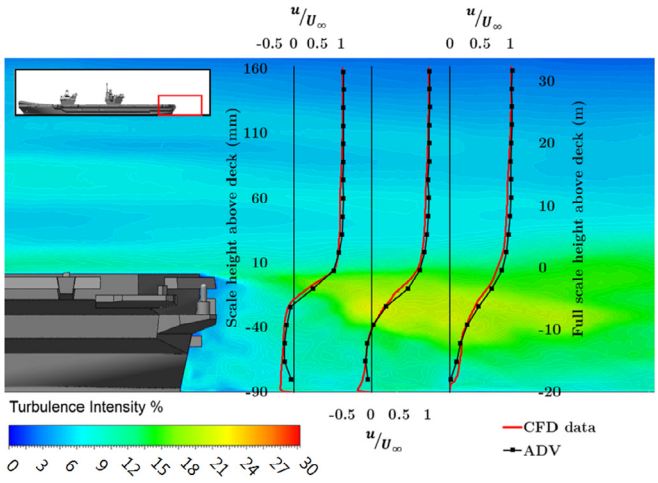

Fig. 10. Comparison of experiment and CFD mean *u*-velocity component astern of the ship centreline.

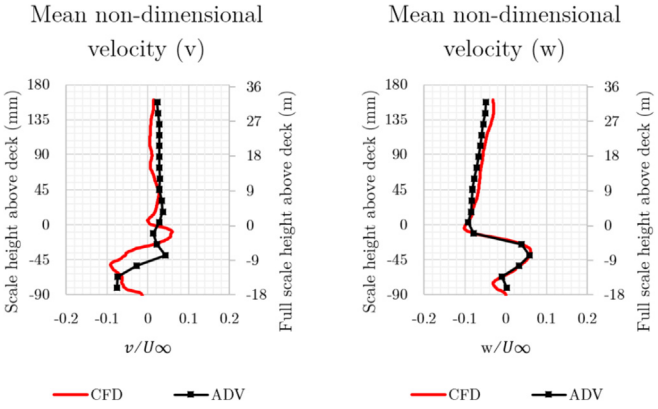

Fig. 11. Comparison of experimental and CFD mean *v*- and *w*-velocity components at the rear of the ship centreline.

CFD and the measured points show reasonably good agreement, given that the velocities are small and will be sensitive to the positional accuracy of the ADV probe.

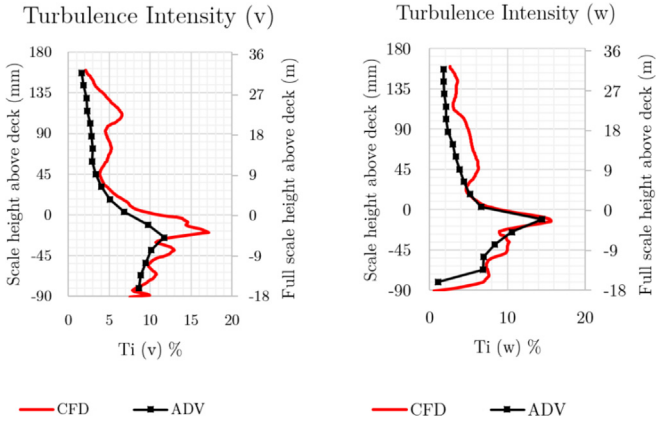

Fig. 12. Comparison of experimental and CFD turbulence intensities in *v*- and *w*-velocity components at the rear of the ship centreline.

Fig. 12 shows the turbulence intensities corresponding to the mean velocities in Fig. 11. The peak in the turbulence coincides with the shear layer indicated in Fig. 10; again, the agreement between experiment and CFD is reasonably good.

The bow of the ship is also interesting from an aerodynamic perspective. Looking at the front of the ship in Fig. 1 it appears to be blunt, but the leading edges of the flight deck-edge are rounded with a full-scale radius of 1 m. Turbulent flow cascading down the flight deck from separation at the bow can potentially impact aircraft operating downstream. Czerwiec and Polsky (Czerwiec and Polsky, 2004) investigated the unsteady flow over the flight deck of a Landing Helicopter Assault ship, which had a square leading edge. Wind tunnel tests and CFD showed that the flow over the deck was significantly improved by attaching a downward-deflected flap to the ship's bow. Bardera et al. (Bardera et al., 2017) conducted an experimental wind tunnel study of the flow over an aircraft carrier's ski-jump, which had a leading edge that was relatively sharp, and showed that a significant flow separation took place. As discussed earlier, the small-scale QEC model can be expected to exhibit flow separation at the bow and, with careful scrutiny, this can be seen in the CFD results in Fig. 13, which shows the *u*-velocity along various vertical lines on a plane through the centre of the ski-jump, and which also shows that there is a separation bubble over the ski-jump.

The outline of the ski-jump may resemble that of an aerofoil, but its purpose is to impart an upward vertical velocity and ballistic profile to the aircraft, providing additional time to accelerate to flying speed whilst ensuring it is on a safe trajectory. This additional time leads to either a reduced take-off length for a given weight, or an increased weight for a fixed take-off distance. The take-off benefits have to be

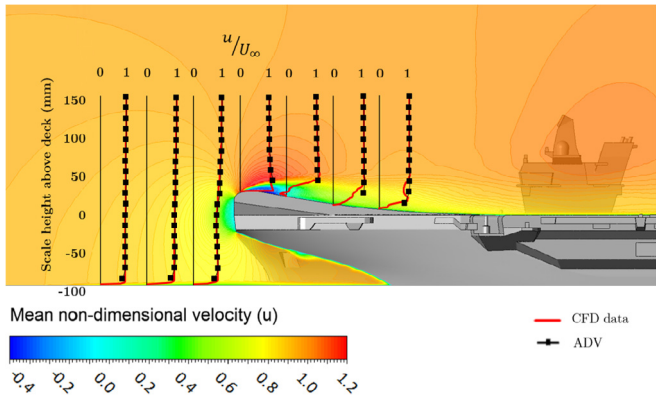

Fig. 13. Comparison of experiment and CFD *u*-velocity over the ski-jump.

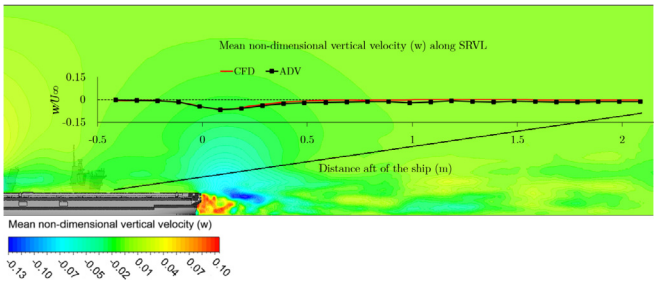

Fig. 14. Comparison of experiment and CFD mean *w*-velocity along the SRVL approach path.

balanced against the significant additional loads that are imparted to the landing gear and so the ramp profile is a balance between these two requirements (Fry et al., 2009). The presence of flow separation over the ramp (or from the leading edge of the flight deck to the starboard of the ramp) will largely depend on the radius of the leading edge and on the flow Reynolds number (Cooper, 1985). As the Reynolds number reduces, the radius of the rounded edge must be increased to maintain attached flow (Hucho et al., 1976). As indicated earlier, it was expected that the small-scale headwind flow would demonstrate separation, while the full-scale would not.

As well as the flow directly over the ship, it is also important that the flow astern of the ship is well modelled and validated, where the challenge for the CFD is to maintain the turbulent eddies in the airwake for a significant distance downstream, covering the fixed-wing approach path. While conventional fixed-wing carrier-borne aircraft approach the carrier on a nominally 3° glideslope (Urnes et al., 1981), the F-35B aircraft will approach along a steeper 7° glideslope during SRVL (Cook et al., 2010), thus passing higher over the stern of the ship.

Fig. 14 shows the vertical *w*-velocity component plotted along the SRVL approach path; in this case the vertical plane corresponds with the centreline of the ski-jump, since that is the pilot's line-up reference cue. For the experiments, the traverse system was programmed to collect velocity measurements along the approach path. As can be seen in Fig. 14 there is a downward velocity component at the stern of the ship, as seen earlier in Fig. 11; a feature known colloquially as the "burble" (NAVAIR, 2009).

The experimental and computed streamwise, *u*, and lateral, *v*, mean velocity components along the glideslope are compared in Fig. 15. Away from the direct influence of the ship the *u*-velocity component is essentially 1 m/s for both the experiment and the CFD. The lateral velocity component is close to zero, with some influence of the

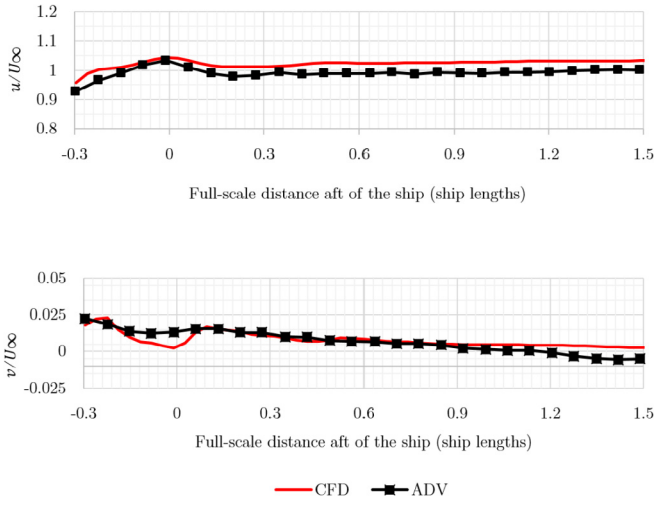

Fig. 15. Comparison of experiment and CFD mean *u*- and *v*-velocity components along the SRVL approach path.

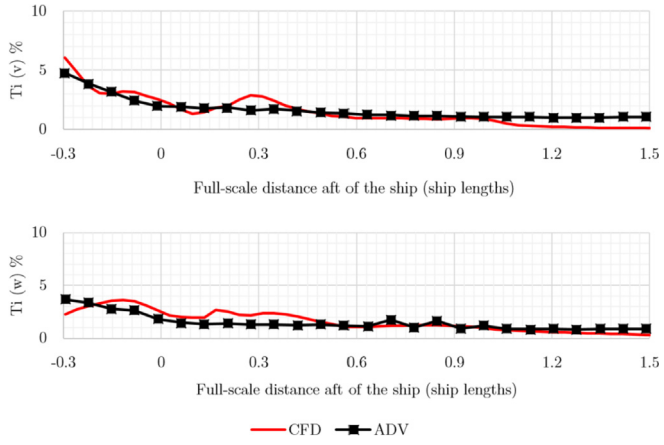

Fig. 16. Comparison of experimental and CFD turbulence intensities in *v*- and *w*-velocity components along the SRVL approach path.

asymmetry of the ship apparent.

Fig. 16 shows the comparison of experimental and CFD turbulence intensities in the lateral, *v*, and vertical, *w*, velocity components along the SRVL approach path. The agreement is reasonable, and the experimental values fall away towards the freestream value of approximately 1% after one ship length astern. It can be seen that despite the efforts taken to prevent turbulence dissipation, the computed turbulence does fall towards zero from around 1.2 ship lengths astern.

4.2. Green 10° wind

For the orientation of the ship that corresponded to a 10° starboard wind, commonly referred to as a Green 10° wind, a similar level of agreement between the experiment and the CFD was found, so only a limited set of data is presented below. Fig. 17 illustrates the airwake using instantaneous Q-criterion isosurfaces. The wake from the islands can be seen spreading across the flight deck, and there are vortical structures which pass along the deck and over the VL spots from the side of the ski-jump, which is no longer aligned with the incoming wind.

Fig. 18, comparable to Fig. 8 for the headwind case, shows the agreement between the experimental measurements of mean *u*-velocity component and the computed values. As already defined, the direction of the *u*-component is parallel to the axis of the ship, so the ADV probes were carefully rotated to an angle of 10° to the flow and the traverse was programmed to follow the vertical plane through the centre of the islands while the ship was yawed at 10°. The velocity components from

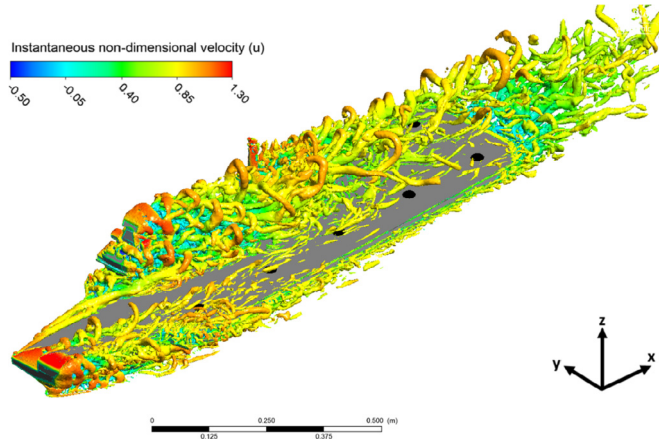

Fig. 17. Flow over QEC model presented as instantaneous isosurfaces of Q-criterion coloured by *u*-velocity.

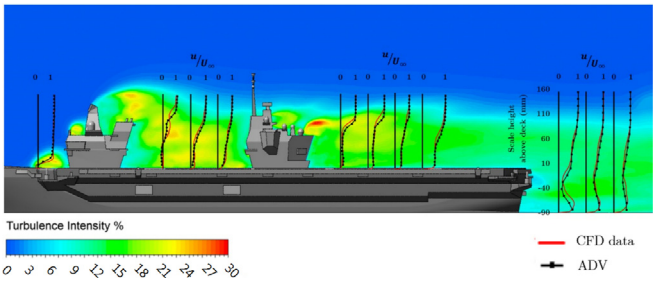

Fig. 18. Comparison of experimental and CFD *u*-velocity components in plane through centre of islands.

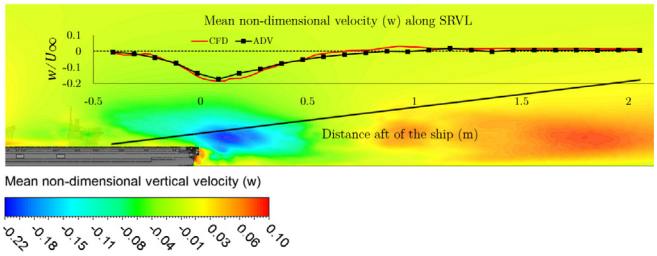

Fig. 19. Comparison of experiment and CFD mean *w*-velocity along SRVL approach path.

the CFD were similarly transformed. As can be seen in Fig. 18, the agreement between the CFD and the experiment is good, although slightly less so along the vertical lines immediately aft of the islands and the stern of the ship, where there will be a greater effect on the airwake due to the oblique flow.

The *w*-velocity component measured along the SRVL approach path is shown in Fig. 19; there is again a good agreement between the CFD and the experiment. The maximum downward velocity component is 0.17 m/s, compared with 0.066 m/s in the case of the headwind, a feature that should be noticeable to pilots when the airwakes are integrated into the flight simulator.

Overall for the small-scale study, the average differences between the computed and measured velocities was less than 5%.

5. Full-scale CFD study

While the small-scale CFD study reported in the previous section modelled the flow in the confined working section of the water channel, the full-scale CFD is on a much larger scale; not just because of the size of the ship, but also the necessary size of the computational domain in which it is placed. As discussed earlier, the reason for creating the airwakes is partly to provide information on the flow over the QEC flight deck, but primarily to provide unsteady air flow data for integration into the BAE Systems and UoL flight simulators. Therefore, the CFD computational domain needs to be much larger than the volume in which the aircraft will actually fly during launch and recovery manoeuvres.

The CFD domain for the full-scale QEC is shown in Fig. 20. The cylindrical geometry allows the wind angle to be varied through 360° by changing the *u* and *v* components of the freestream velocity without having to alter the computational domain. The rectangular focus region (red box) around the ship is the volume in which the aircraft will experience the airwake disturbances in the simulator, shown earlier in Fig. 2; the box has a length of 700 m, a width of 200 m and a height of 72 m, and within this the grid size was limited to 1 m.

The overall CFD domain in Fig. 20 needs to be large enough to ensure that boundaries are kept at a sufficient distance from the rectangular volume to avoid interfering with the flow computations. The CFD computational domain height was set at 0.75 ship length (210 m),

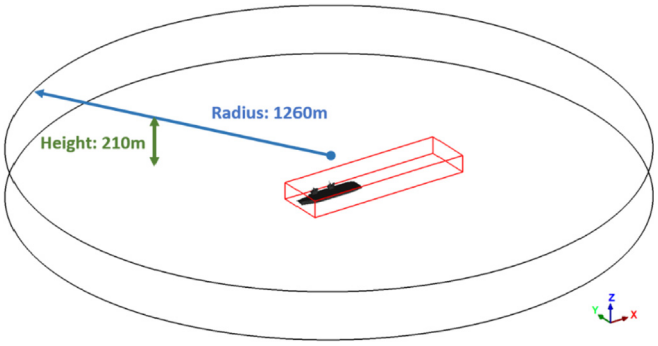

Fig. 20. Computational domain for CFD including rectangular focus region.

while the radius was set to 4.5 ship lengths (1260 m), placing the ship geometry and the rectangular box at a sufficient distance from far-field boundaries to ensure that the fluid flow in the focus region is not impacted by unphysical effects which may occur near to the domain boundaries; the dimensions of the cylindrical domain are consistent with the approach used by Forrest and Owen for smaller ships (Forrest and Owen, 2010).

The surface elements on the full-scale ship were triangular with a side length of 0.3 m, and surface features on the ship smaller than 0.5 m were removed (e.g. handrails, aerials and antenna etc.). Similar to the small-scale ship, twelve layers of prism elements were grown from the surface to resolve the viscous boundary layer. The overall cell count was approximately 100 million. Fig. 21 shows the actual time to create a full-scale airwake when using 256 processors in an HPC cluster; the progress of the solution was monitored by recording the velocity components at several points in the flow. The initial steady-state solution took around 12 h, the settling period was in the region of 9 days and the time for computing the 30 s of unsteady airwake required for export to the flight simulator was a further 12 days, giving a total time of approximately three weeks. The unsteady solution was computed using a time step of 0.01 s (100 Hz).

Unlike the small-scale CFD, where a uniform velocity profile was applied to the inlet of the CFD domain, for the full-scale model an inlet velocity profile was applied representing the oceanic Atmospheric Boundary Layer (ABL) using Eqn. (3), where: V_{ref} is the reference windspeed measured at a known height above sea-level, z_{ref}, and z_0 is the sea-surface roughness length-scale which, according to Garratt (Garratt, 1994), can be taken to equal 0.001 m for oceanic conditions.

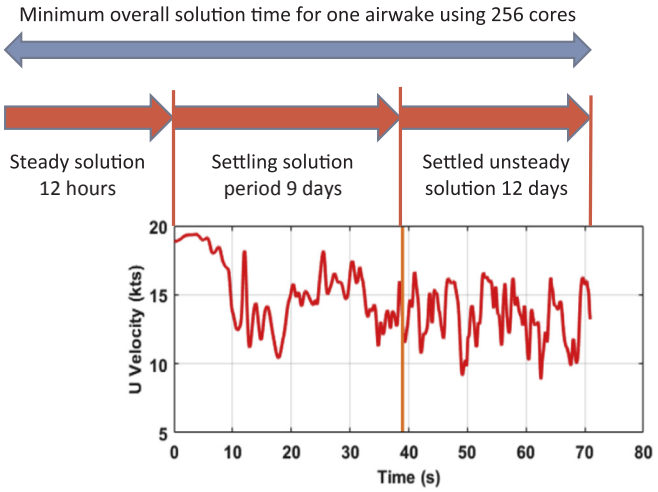

Fig. 21. Sampled airwake velocity used for monitoring progress of unsteady solution.

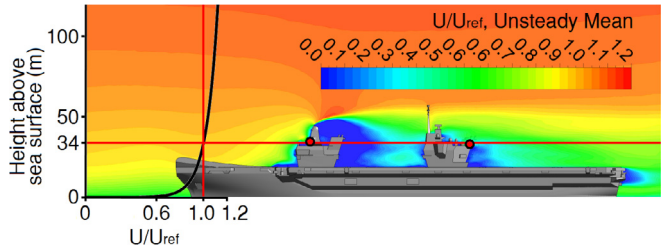

Fig. 22. Contours of mean normalised *u*-velocity components in a plane through the centre of the islands, including the ABL inlet profile.

$$V = V_{ref}\left(\frac{\ln(\frac{z}{z_0})}{\ln(\frac{z_{ref}}{z_0})}\right) \quad (3)$$

The reference wind speed, V_{ref}, is the desired wind speed at the mean height of the ship's anemometers.

Similar to the small-scale model, all surfaces of the carrier were modelled as zero-slip walls. The upper surface of the domain was set as a pressure-far-field, allowing static pressure to be specified at the boundary, and thus minimising any potential blockage effects. Unlike the water tunnel floor, the sea surface was set as a wall with a slip condition, thereby allowing the prescribed ABL to be maintained throughout the domain.

Fig. 22 shows the computed full-scale airwake for a headwind as contours of the mean *u*-velocity; the vertical plane is through the centre of the islands. Also included in this figure is the ABL velocity profile ahead of the ship. While in the small-scale study it was possible to characterise the inlet flow by the uniform inlet velocity (1 m/s), in the full-scale case the inlet flow is described by the velocity at the mean height of the ship's three island-mounted anemometers, which is approximately 34 m above the sea surface. The velocity at anemometer height in Fig. 22 is 25 knots (12.86 m/s).

Considering the different inlet velocity profiles used for the full- and small-scale cases, a difference between the normalised airwakes is expected; and, as discussed earlier, the different Reynolds numbers (on the order of 10^6 at small-scale compared with 10^8 at full-scale) are also expected to have an effect on the separation of the air flow at the bow. Fig. 23 shows a comparison of the full- and small-scale CFD at various locations in a plane through the centre of the islands for a headwind; the full-scale CFD has been normalised by the velocity at the anemometer height; turbulence contours are those for the small-scale ship. Ahead of the forward island and between the two islands there is some difference between the profiles of the *u*-velocity component which is probably a result of the ABL inlet profile. The velocity profiles in the lee of the aft island and astern of the ship are very similar and this is probably because in this region the flow has been well mixed and the influence of the ABL has dissipated.

Fig. 24 shows a comparison of the full-scale and small-scale CFD results over the ski-jump at the bow of the ship. As discussed previously, due to the curved profile of the leading edge of the ski-jump, it can be expected that flow separation will be affected by the difference

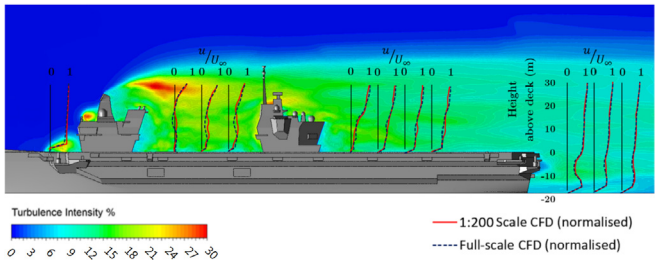

Fig. 23. Comparison of small-scale and full-scale CFD results in *u*-velocity component.

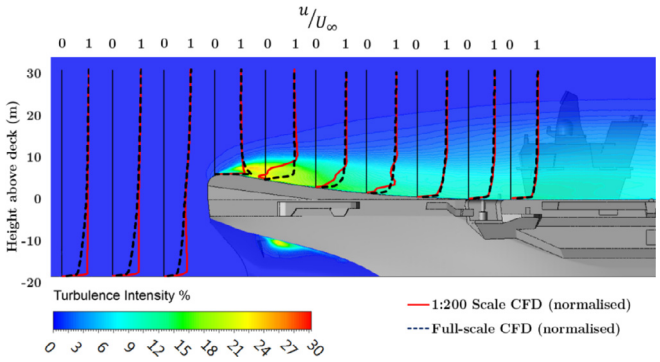

Fig. 24. Comparison of full-scale and small-scale CFD results in *u*-velocity component over the ski-jump.

in Reynolds number at full-scale and small-scale, in addition to the presence of an ABL in the full-scale solution. As can be seen in Fig. 24 there is no evidence of a separation bubble in the full-scale flow, and towards the end of the ski-jump the two velocity profiles are comparable. Furthermore, although not shown here, the full- and small-scale velocity profiles further down the flight deck and over the landing spots are very similar. Fig. 25 shows computed mean streamlines over the bow of the ship in a headwind, demonstrating the smooth air flow and the effectiveness of the bow design.

A further comparison between the small- and full-scale CFD is shown in Fig. 26, for the Green 10° wind direction. As before, the direction of the *u*-velocity component is parallel to the centreline of the ship; again the two flows are very similar.

5.1. Air flow over the full-scale flight deck

Fig. 27 shows the mean air flow over the QEC in a headwind, illustrated by mean streamlines in vertical planes that are aligned with the oncoming wind and pass through the landing spots (spots 1 to 5 along the length of the deck and spot 6 behind the aft island). The streamlines are coloured by turbulence intensity. The figure also contains contours of turbulence intensity in a horizontal plane that is located 10 m above the flight deck; the significance of the 10 m is that this is the approximate height of the centre of gravity for both fixed- and rotary-wing aircraft when translating across the deck during a vertical landing, according to (Denham et al., 2002). As can be seen, in the headwind case there is little turbulence over the deck at 10 m and spots 1 to 5 are in largely undisturbed air flow.

While it is preferable to launch and recover aircraft to the ship in a headwind, where there will be less flow disturbance over the flight deck and higher relative air speeds, and hence lift for the aircraft, there will inevitably be times when the relative wind will be from directions other than ahead. It is important, therefore, to have an understanding of the air flow over the deck for all wind directions.

For winds from the starboard side of the ship, or Green winds, one

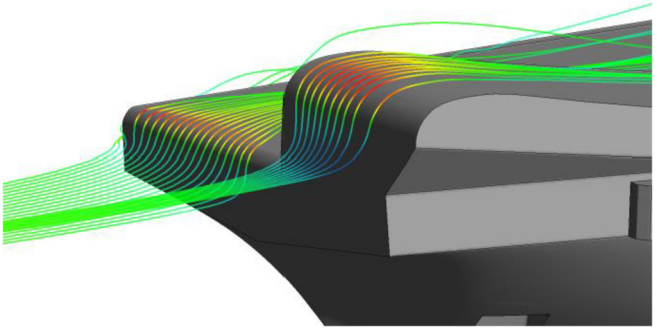

Fig. 25. Mean streamlines over the full-scale bow in a headwind.

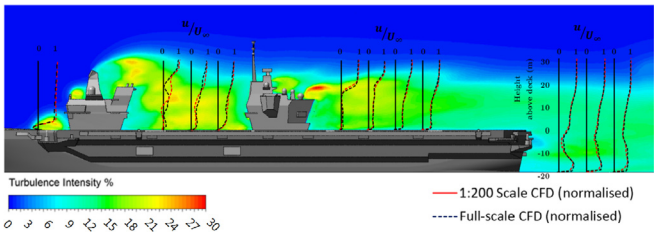

Fig. 26. Comparison of small-scale and full-scale CFD results in u-velocity component. Green 10° wind.

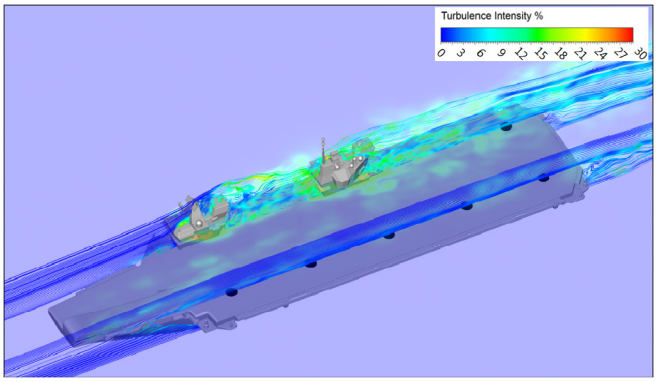

Fig. 27. Full-scale airwake for a headwind as streamlines in vertical planes through the landing spots and turbulence intensity contours in a horizontal plane 10 m above the deck.

might expect increased levels of turbulence over the flight deck due to the effect of the air flowing over and around the island superstructures. Fig. 28 shows examples of the ship airwakes over the flight deck from relative angles Green 25°, Green 45° and Green 90° (beam wind). In these wind conditions the disturbed air flow from the two islands does indeed create more turbulence in the horizontal plane 10 m above the deck. The different orientation of the ship in each figure is to assist the reader in viewing each of the images.

Overall, it can be seen that as the wind moves around to the starboard, the profile presented by each island to the oncoming air flow is increasing, as is the width of the turbulent wake behind each island. By referring to Fig. 2, it can be seen that the vertical landing approach requires the aircraft, fixed- and rotary-wing, to come alongside the ship on the port-side, hold a hover position alongside the designated landing spot by matching the ship's forward speed, and to then translate sideways across the port deck-edge to the hover position above the landing spot, before descending to the deck. Therefore, the nature of the air flow off the port-side and over the flight deck is an important contributor to the aircrafts' perceived handling qualities and pilot workload. Taking the three images in Fig. 28 together, it can be seen that as the wind moves from ahead to abeam, so the turbulent flow from the islands encroaches on more landing spots, becomes more turbulent at each landing spot, and more turbulent off the port-side. It can, therefore, naturally be concluded that Green winds will increase pilot workload during vertical landings at each spot, a result which is consistent with historical experience for an aircraft carrier with superstructure on the starboard side of the flight deck. The CFD results clearly illustrate why Green winds increase pilot workload compared to headwinds or Red winds.

The beam wind in Fig. 28 shows how the flow separating from the sides of the islands creates turbulent air in the vicinity of spots 1 to 4; where 25%–30% turbulence intensity represents a significant disturbance. The islands also deflect the flow upwards and it can be seen that the separated flow over the forward island reattaches near to spot 1; bearing in mind that the flow is represented by mean streamlines this means that the reattachment point and the flow direction at spot 1 could be fluctuating significantly. The flow deflected upwards from the aft island does not reattach to the deck and produces an area of highly turbulent air flow, although the most turbulent flow is 30 m above the deck and above the height of normal flying operations. Although spots 5 and 6 at the stern of the ship are not in the wake of the islands, the air flow separating from the starboard deck-edge of the ship still causes significant turbulence, particularly over spot 5 on the port side. The beam winds will also create significant turbulence off the port-side of the ship where the aircraft will take up their hover position before translating across the deck to the landing spot.

In contrast, referring to Fig. 29, Red winds (winds from the port) create much less turbulence over the flight deck and will, therefore, be more favourable than Green winds. The possible exception is at spot 1, near the ski-jump, where the air flow in 25° and 45° Red winds could be affected by the corner formed by the deck-edge and the forward bow section. However, the Red 90 winds still creates significant turbulence due to the flow separating from the ship's port deck-edge and, interestingly, the islands still have a significant influence on the flow over the flight deck. The combined effect of the two islands deflecting flow upwards means that the flow separating from the port deck-edge does not reattach on the flight deck, except at spots 5 and 6 where the flow reattaches around one-third of the way across the flight deck. The channelling effect of the two islands can also be seen in the vertical plane through spot 2, where there is a large region of flow with turbulence intensities of 30%.

As described at the beginning of this paper, the full-scale unsteady airwakes have been primarily computed for integration with the BAE Systems and UoL piloted flight simulators, and although the general characteristics of the flow over the deck can be described and commented upon as they have been above, the effect of the airwake on the aircraft and on pilot workload can only be assessed by trained test pilots either in the simulator or during real at-sea flight trials. Pilots are trained to operate in the challenging conditions encountered around the ship, including air turbulence and deck motion. Modern military aircraft, particularly the F-35B, have highly augmented flight control systems which are designed to alleviate pilot workload (Denham, 2016). Nevertheless, it is clear from the airwake data presented here that the most favourable conditions under which to perform a vertical landing is in a headwind, when the disturbed air flow from the islands is least influencing the flow over spots 1 to 5, although it will affect spot 6. It has been shown that the rounded leading edges of the ski-jump and the adjacent deck-edge allows the flow from ahead to remain attached and to create only a small disturbance along the length of the flight deck. It can also be deduced that Red winds are preferable to Green winds, and that the closer Green winds approach beam winds, the more problematic they become for aircraft operations.

6. Conclusions

This paper has reported a selection of results from a detailed and extensive modelling study of the air flow over and around the Queen Elizabeth Class aircraft carriers. Comprehensive knowledge of the air flow for different wind speeds and directions is important for understanding the aerodynamic environment around the ship, and for creating detailed and realistic simulations which can be used to inform ship superstructure design and at-sea flight trials.

The ship airwake is highly dynamic and the unsteady flow field will at some stage impact on aircraft operations to the ship. It is therefore essential that time-accurate CFD is used to model the airwake. This study has demonstrated that Delayed Detached Eddy Simulation is an effective CFD technique for this task. In applying the DDES technique it is important that a settling period is included to allow the unsteady flow to become ‘settled’. It is also important that cell growth is limited in areas of interest so that turbulent kinetic energy dissipation is minimised.

The validity of the CFD approach was confirmed by experiment in

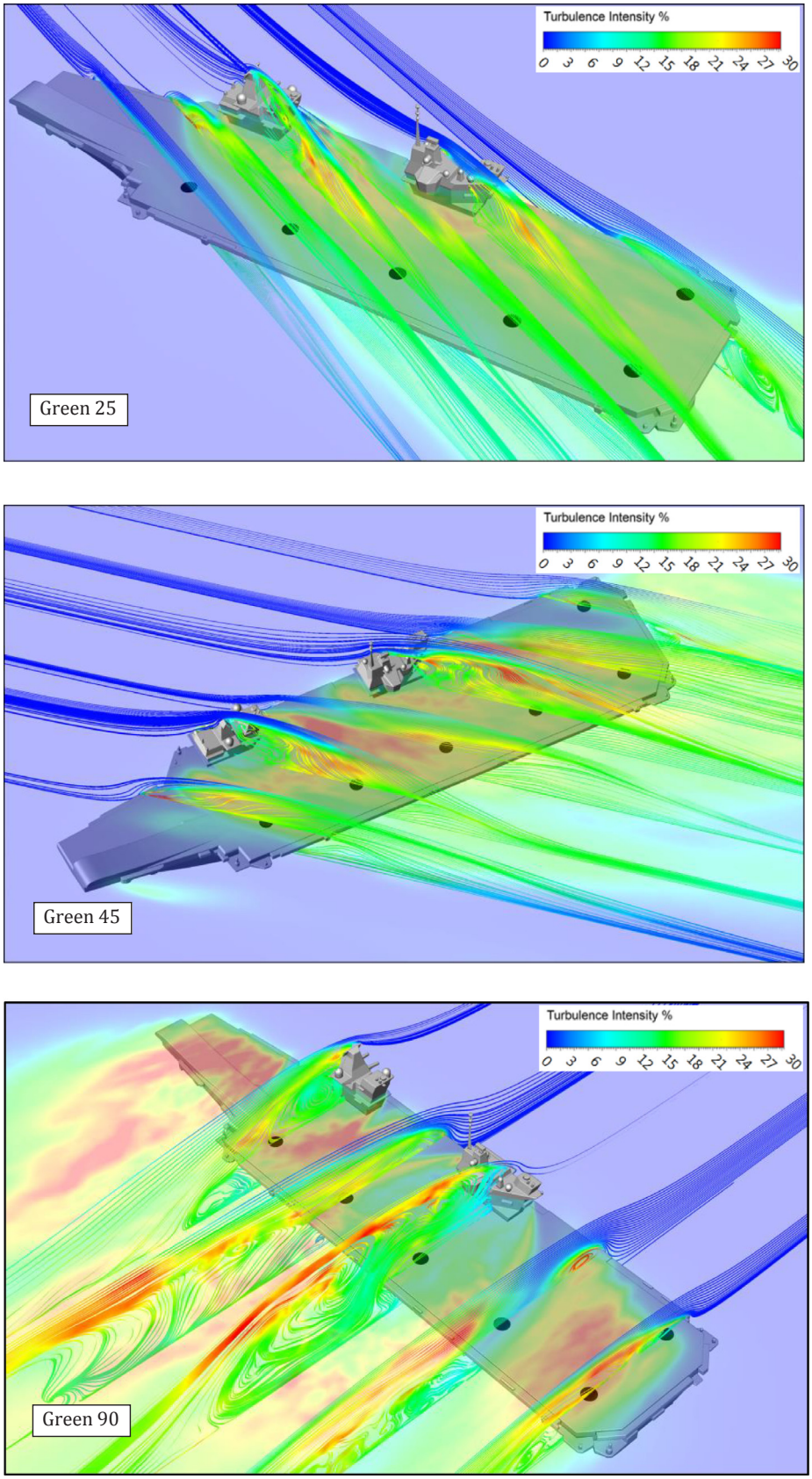

Fig. 28. Full-scale airwakes for starboard winds illustrated as streamlines in vertical planes through landing spots and turbulence intensity contours in horizontal plane 10 m above deck.

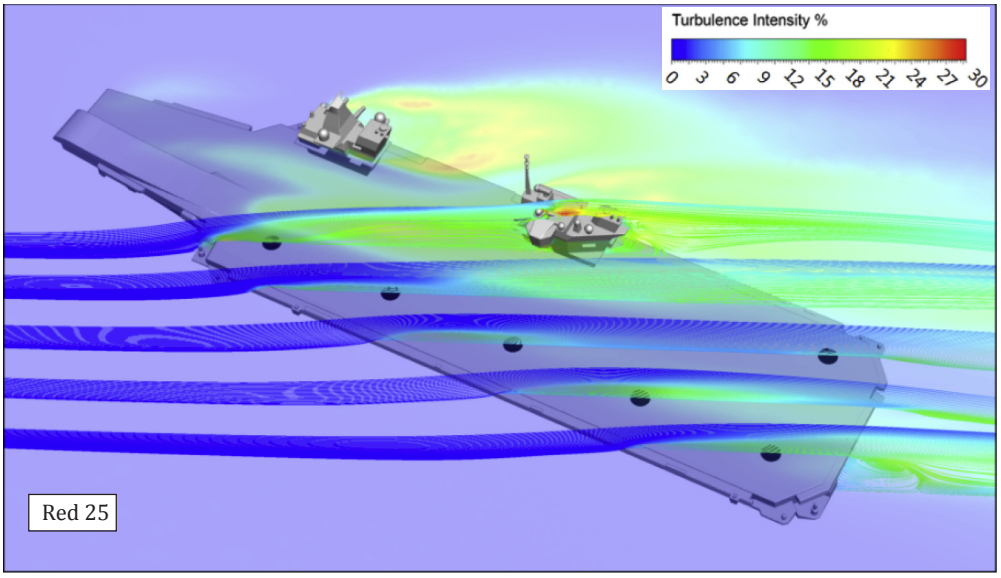

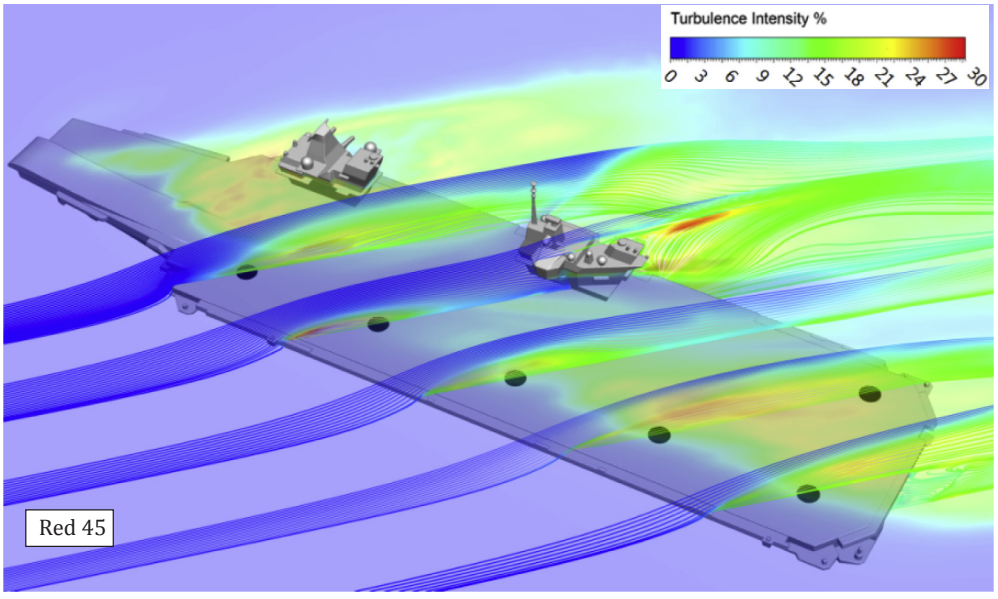

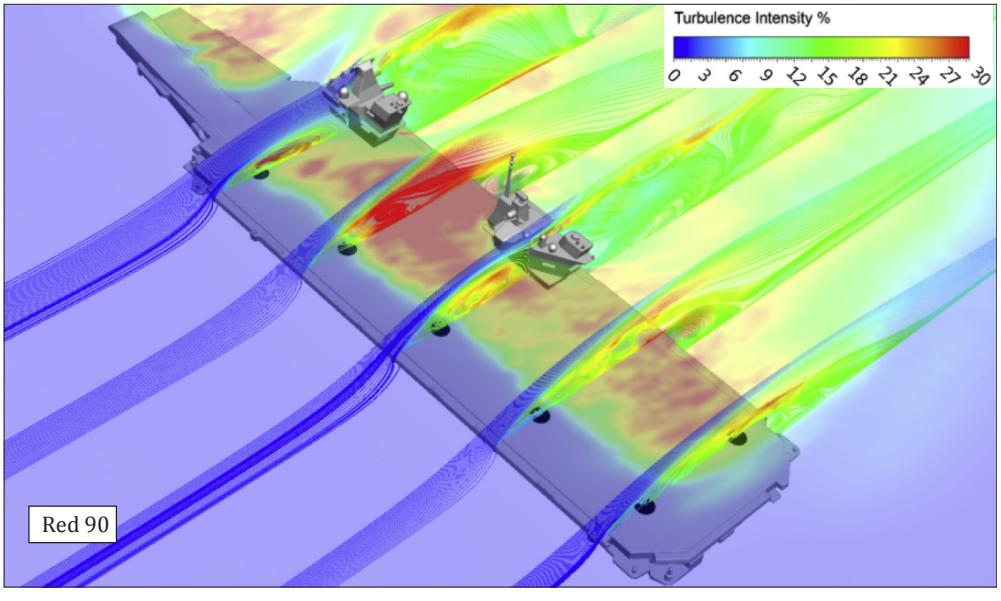

(caption on next page)

Fig. 29. Full-scale airwakes for port winds illustrated as streamlines in vertical planes through landing spots and turbulence intensity contours in horizontal plane 10 m above deck.

two stages: first the CFD technique was applied at the same small-scale conditions as the water channel experiment, and then the CFD was applied to the full-scale conditions. Overall, the small-scale experiment and CFD showed excellent agreement; average differences between measured and computed velocities were mostly less than 5%.

Traditionally, wind tunnel experiments have been used to measure and visualise the flow field around ships and the data has then been scaled to represent the full-scale flow field. Comparison of the small-scale experiment and the full-scale CFD showed reasonable agreement, despite differences in Reynolds number and the inlet velocity profiles. This observation suggests that the full-scale CFD is at least as representative of the full-scale situation as the small-scale experiment, and that it is an effective tool for simulating the full-scale air flow over a large structure, such as an aircraft carrier.

Ship airwake experiments are normally performed in wind tunnels, employing instrumentation such as pitot probes, hot wire anemometry, laser Doppler anemometry, or particle imaging velocimetry. This study has shown that a water channel (or tunnel) is an effective alternative and that an Acoustic Doppler Velocimeter, not normally used for detailed studies such as reported here, is a very effective instrument.

The characteristic design features of the QEC aircraft carriers are the twin island superstructure and the ski-jump situated at the bow. Aerodynamically, the twin islands have been shown to create some complex airflows over the flight deck in oblique winds, while the rounded profiles of the ski-jump and the adjacent bow area allows the flow to remain attached to the deck surface and will not create significant flow disturbances along the flight deck for winds from ahead. The air flow being shed from the islands in starboard winds can be expected to create more challenging flying conditions, as is normally the case for aviation-capable ships.

Acknowledgements

The Authors acknowledge the financial support from the Engineering and Physical Sciences Research Council through Industrial CASE Awards jointly funded with BAE Systems, and the ongoing support of ANSYS UK Ltd.

References

ANSYS Inc, 2016. ANSYS Fluent 16.2 User Guide. Canonsburg, PA.
Atkinson, D., Brown, R., Potts, R., Bennett, D., 2013. Integration of the F-35 joint strike fighter with the UK queen Elizabeth class Aircraft Carrier. In: Proceedings of the International Powered Lift Conference, Los Angeles, California.
Bardera, R., Rodríguez-Sevillano, A., León-Calero, M., Nova-Trigueros, J., June 2017. Three-dimensional characterization of passive flow control devices over an aircraft Carrier ski-jump ramp. In: Proceedings of the Institution of Mechanical Engineers, Part G: Journal of Aerospace Engineering, pp. 1–8 0(0).
Bevilaqua, P.M., January 2009. Inventing the F-35 joint strike fighter. In: 47th AIAA Aerospace Sciences Meeting Including the New Horizons Forum and Aerospace Exposition, Orlando, Florida. AIAA 2009-1650.
Chanson, H., Trevethan, M., Koch, C., November 2007. "Discussion of 'turbulence measurements with acoustic Doppler velocimeters" by Carlos M. García, Mariano I. Cantero, Yarko Niño, and Marcelo H. García". J. Hydraul. Eng. 133 (11), 1283–1286.
Cook, R., Atkinson, D., Milla, R., Revill, N., Wilson, P., 2010. Development of the Shipborne rolling vertical landing (SRVL) manoeuvre for the F-35B aircraft. In: Proceedings of the International Powered Lift Conference, Philadelphia, PA.
Cooper, K.R., February 1985. The Effect of Front-edge Rounding and Rear-edge Shaping on the Aerodynamic Drag of Bluff Vehicles in Ground Proximity. SAE Technical Paper 850288.
Czerwiec, R.M., Polsky, S.A., August 2004. LHA airwake wind tunnel and CFD comparison with and without bow flap. In: 22nd Applied Aerodynamics Conference and Exhibit, Guidance, Navigation, and Control and Co-located Conferences, Rhode Island, AIAA Paper 2004-4832.
Denham, J.W., Jan 2016. Project MAGIC CARPET: Advanced controls and displays for precision carrier landings. In: Presented at the 54th AIAA Aerospace Sciences Meeting, San Diego, California.
Denham, J.W., Krumenacker, J.L., D'Mello, G.W., Lewis, M., January 23-25, 2002. Taking Advanced STOVL Flight Control to Sea: the VAAC Follow-on Research Programme. In: Presented at the American Helicopter Society Aerodynamics, Acoustics, and Test and Evaluation Technical Specialists Meeting, San Francisco, CA.
Engineering Sciences Data Unit, 1978. Fluid Forces, Pressure and Moments on Rectangular Blocks. ESDU Data Item 71016.
Forrest, J.S., Owen, I., April 2010. Investigation of ship airwakes using detached-eddy simulation. Comput. Fluids 39 (No. 4), 656–673.
Forrest, J.S., Kääriä, C.H., Owen, I., October 2016. Evaluating ship superstructure aerodynamics for maritime helicopter operations through CFD and flight simulation. Aeronaut. J. 120 (issue 1232), 1578–1603.
Fry, A., Cook, R., Revill, N., February 2009. CVF ski-jump ramp profile optimisation for F-35B. Aeronaut. J. 113 (issue 1140), 79–85.
Garratt, R., April 1994. The atmospheric boundary layer. In: Cambridge Atmospheric and Space Science Series. Cambridge University Press.
Hodge, S.J., Wilson, P.N., July 2008. Operating JSF from CVF: the reality of simulation. In: Proceedings of the International Powered Lift Conference. RAeS, London.
Hodge, S.J., Forrest, J.S., Padfield, G.D., Owen, I., November 2012. Simulating the environment at the aircraft-ship dynamic interface: research, development, & application. Aeronaut. J. 116 (issue 1158), 1155–1184.
Hucho, W.H., Janssen, L.J., Emmelmann, H.J., February 1976. The Optimization of Body Details – a Method for Reducing the Aerodynamic Drag of Road Vehicles. SAE Technical Paper 760185.
Hunt, J.C.R., Wray, A.A., Moin, P., 1988. Eddies, streams, and convergence zones in turbulent flows. In: Proc. 1988 Summer Program, NASA Stanford Center for Turbulence Research, Report CTR-S88, pp. 193–208.
Kraus, N.C., Lohrmann, A., Cabrera, R., March 1994. New acoustic meter for measuring 3d laboratory flows. J. Hydraul. Eng. 120 (3), 406–412.
Lane, S.N., Biron, P.M., Bradbrook, K.F., Butler, J.B., et al., December 1998. Three-dimensional measurements of river channel topography and flow processes using acoustic Doppler velocimetry. Earth Surf. Process. Landforms 23 (13), 1247–1267.
Lison, A., June 2009. Integrating the Joint Combat Aircraft into the Queen Elizabeth class aircraft carriers – Design challenge or opportunity? In: Warship 2009 – 'Airpower at Sea', London, UK.
Lohrmann, A., Cabrera, R., Kraus, N., August 1994. Acoustic-Doppler Velocimeter (ADV) for laboratory use. In: Fundamentals and Advancements in Hydraulic Measurements and Experimentation. American Society of Civil Engineers, Buffalo, New York.
Lopez, F., Garcia, M.H., May 2001. Mean flow and turbulence structure of open-channel flow through nonemergent vegetation. J. Hydraul. Eng. 127 (5), 392–402.
Menter, F.R., Kuntz, M., 2004. Adaptation of eddy-viscosity turbulence models to unsteady separated flow behind vehicles. In: In: McCallen, R., Browand, F., Ross, J. (Eds.), The Aerodynamics of Heavy Vehicles: Trucks, Buses, and Trains. Lecture Notes in Applied and Computational Mechanics, vol. 19 Springer, Berlin, Heidelberg.
Millward, A., Nicholson, K., Preston, J.H., September 1980. The use of jet injection to produce uniform velocity in a high speed water channel. J. Ship Res. 24 (2), 128–134.
NAVAIR, May 2009. NATOPS Landing signal officer manual. In: US Naval Air Systems Command, NAVAIR-00-80T-104.
Owen, I., White, M.D., Padfield, G.D., Hodge, S.J., December 2017. "A virtual engineering approach to the ship-helicopter dynamic interface – a decade of modelling and simulation research at the University of Liverpool". Aeronaut. J. 121 (Issue 1246), 1833–1857.
Roper, D.M., Owen, I., Padfield, G.D., Hodge, S.J., February 2006. Integrating CFD and piloted simulation to quantify ship-helicopter operating limits. Aeronaut. J. 110 (1109), 419–428.
Royal Navy Imagery Database, accessed March 2018, https://www.royalnavy.mod.uk/useful-resources-and-information/rn-image-archive.
Spalart, P.R., August 1997. Comments on the feasibility of LES for wing and on a hybrid RANS/LES approach. In: 1st ASOSR Conference on DNS/LES. Arlington, TX.
Spalart, P.R., 2001. Young-Person's Guide to Detached-eddy Simulation. NASA Report: NASA/CR-2001-211032, July.
Spalart, P.R., Deck, S., Shur, M.L., Squires, K.D., Strelets, M. Kh, Travin, A., July 2006. A new version of detached-eddy simulation, resistant to ambiguous grid densities. Theor. Comput. Fluid Dynam. 20 (181), 181–195.
Urnes, J.M., Hess, R.K., Moomaw, R.F., March-April 1981. H-dot automatic Carrier landing system for approach control in turbulence. J. Guid. Contr. 4 (2), 177–183.
Voulgaris, G., Trowbridge, J.H., February 1998. Evaluation of the acoustic Doppler velocimeter (ADV) for turbulence measurements. J. Atmos. Ocean. Technol. 15 (1), 272–289.
White, M.D., Perfect, P., Padfield, G.D., Gubbels, A.W., Berryman, A.C., April 2013. Acceptance testing and commissioning of a flight simulator for rotorcraft simulation fidelity research. In: Proceedings of the Institution of Mechanical Engineers, Part G: Journal of Aerospace Engineering, vol. 227. pp. 663–686 4.